Recycling of Tantalum Capacitors Via Sulfide Chemistry

ORIGINAL RESEARCH ARTICLE

Recycling of Tantalum Capacitors *Via* Sulfide Chemistry

CHARLES BOURY and ANTOINE ALLANORE

The fabrication of tantalum capacitors represents more than 35 pct of the total consumption of metallic tantalum with an increasing demand for the high-technology sector. Tantalum capacitors contain a large concentration of tantalum, and the absence of niobium leads to interesting economic outcomes for potential recycling processes. The article discusses such recycling using sulfur, where an AB_2O_6 crystal structure analogous to the orthorhombic columbite-tantalite series is sulfidized. Sulfide affinities differences between A (Mn, Fe) and B (Nb, Ta) effectively separate the ternary oxide, capitalizing on the distinct chemical properties between A and B elements, in the absence of fluoridic acids. To bypass the fluoride-based chemistry process entirely, a proof of concept of tantalum disulfide (TaS_2) production *via* sulfidation of Ta_2O_5 and its subsequent metallic reduction *via* molten sulfide electrolysis are also presented.

https://doi.org/10.1007/s11663-024-03427-1

I. INTRODUCTION

TANTALUM has unique properties among metals, such as high melting point, mechanical hardness, corrosion resistance, and biological compatibility.[1,2] Tantalum materials, from raw primary feed minerals to metallic products and alloys, are not closely followed through the global economy,[3] leading to an annually estimated 2000 tons of metallic tantalum produced worldwide.[4] Tantalum price volatility stems from supply-demand shifts and geopolitical factors in major supply areas. Technological changes and ethical sourcing concerns further impact these fluctuations as developed by Mancheri *et al.*[5] The tantalum supply chain exhibits numerous bottlenecks and would greatly benefit from recycling technologies as many tantalum-containing products exhibit high concentration in tantalum and often free of niobium, such as capacitors.

The extraction of coltan $(Fe,Mn)(Ta,Nb)_2O_6$ in African countries such as the Democratic Republic of Congo, Rwanda, and Nigeria is mainly artisanal, of small-scale, and reportedly vulnerable to extortion and human trafficking.[6,7] The selective separation of tantalum from other metallic elements, mainly niobium, requires expensive and hazardous hydrometallurgical solutions.[8] As described by Nete *et al.*,[9] two major industrial processes allow the refining of coltan to produce high-purity tantalum potassium fluoride salt (K_2TaF_7) and niobium oxide (Nb_2O_5). Both processes are fluoride-based route (namely the "K-salt" route) producing a high-purity K_2TaF_7, subsequently reduced by metallic sodium (Na) or magnesium (Mg)[1,3] to form a high-purity tantalum metal. The chemical separation of Ta and Nb from their minerals is a complex and difficult process due to their strong chemical similarities. However, the recycling of tantalum-containing products, especially free of niobium, could demonstrate numerous advantages by the definition of a more economical, sustainable, and tailored process than the general "K-salt" route.

Following Padilla *et al.*,[3] the production of tantalum capacitors is expected to represent more than 35 pct of the total consumption of tantalum. The low recycling rate of end-of-life tantalum capacitors is mainly due to the small economic value of tantalum in Waste Printed Circuit Boards (WPCBs) compared to other noble metals (such as copper, gold, and silver). Hydro- and pyro-metallurgical processes recover the noble metals in priority, and the tantalum content is lost or in a slag phase as mixed oxide, making its recovery complex and not economically attractive.[10,11] Ramon *et al.* and Choi *et al.* created different apparatus with high detection accuracy and speed to distinguish and separate Waste Tantalum Capacitors (WTC) from WPCBs before recovering noble metals *via* pyrometallurgy.[12,13] Such apparatuses will not be further discussed herein but are the primary step to envisioning an economically viable

CHARLES BOURY and ANTOINE ALLANORE are with the Department of Materials Science and Engineering, Massachusetts Institute of Technology, 77 Massachusetts Ave, Cambridge, MA 02139. Contact e-mail: allanore@mit.edu
Manuscript submitted July 5, 2024; accepted December 27, 2024.

recycling process. An end-of-life tantalum capacitor process will have a high-quality initial feedstock, identical to the brand-new capacitors used in this study.

As schematized in Figure 1, a tantalum capacitor comprises a sintered pellet of metallic tantalum powder partially oxidized, covered with manganese oxide (MnO_2) by electrodeposition as the cathode. The anode terminal is a metallic tantalum wire placed at the center of the pellet. Two metallic leads allow for the external electrical contacts. Their alloy composition depends on the capacitor model, herein a Cu, Zn, Ni alloy. Graphite paste (C), silver (Ag), and tin (Sn) solders ensure electrical contacts. An epoxy resin mixed with silica (SiO_2) powder, acting as a fire retardant, enrobes the capacitors.

The recycling process presented herein, relying on sulfide chemistry, allows the production of an intermediate tantalum oxide product and a final tantalum metal product *via* electrodeposition. The work of Mineta *et al.*[14] originated the pre-treatment, which consisted of calcination, sonication, crushing, and sieving steps. The calcination formed a ternary oxide $MnTa_2O_6$ phase, an endmember of the tantalite mineral series. The selective sulfidation of the ternary oxide $MnTa_2O_6$ leads to the

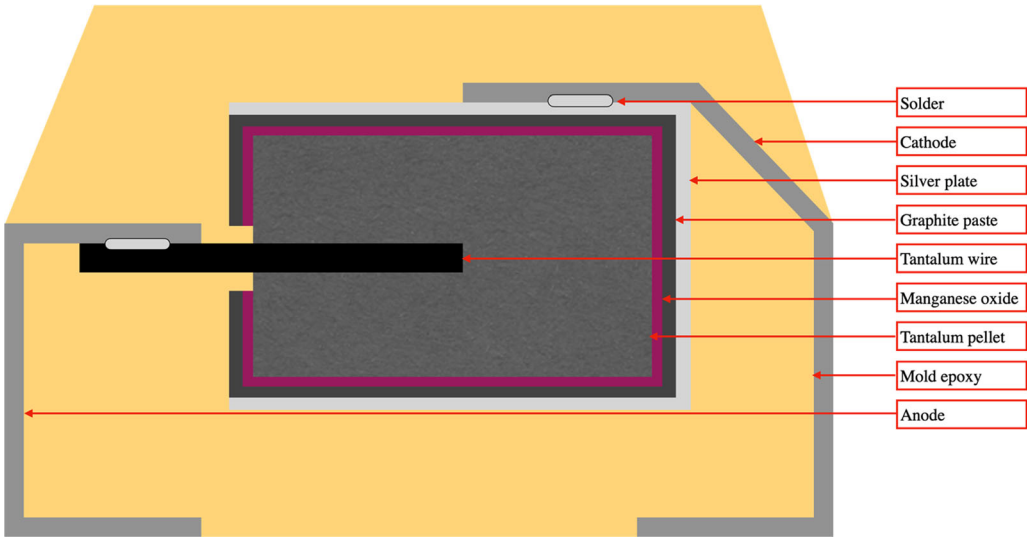

Fig. 1—Schematic of a tantalum capacitor, not to scale.

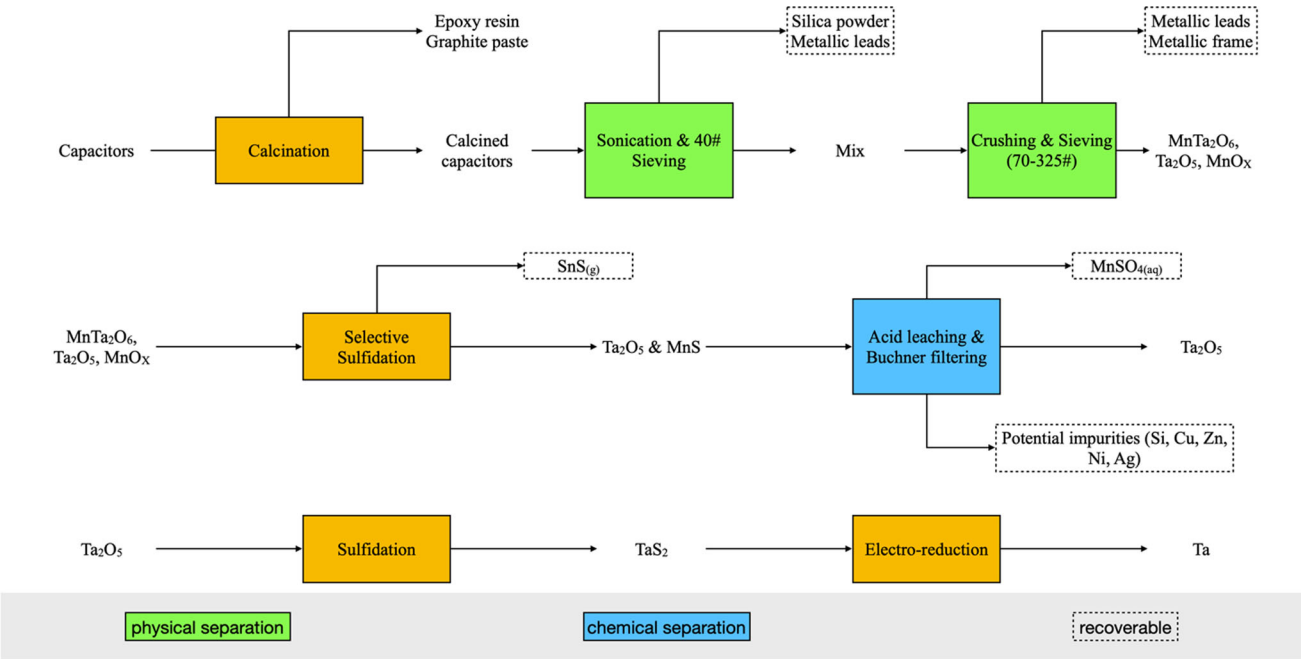

Fig. 2—Schematic of the overall process investigated herein.

mix oxide–sulfide MnS and Ta_2O_5. The nitric acid leaching step removes MnS and impurities, with Ta_2O_5 being insoluble in mild acidic conditions. A proof of concept for the sulfidation of Ta_2O_5 into TaS_2 and tantalum metal production *via* molten sulfide electrolysis is also presented by the authors to offer a potential alternative to the fluoride-based "K-salt" route.

Over the years, several research groups have proposed different solutions to extract and purify tantalum from such capacitors. Agrawal *et al*. submitted a review of the existing and potential recycling routes for waste tantalum capacitors.[15] Mineta and Okabe developed a high-temperature oxidation treatment followed by a hydrometallurgical process and a magnesiothermic

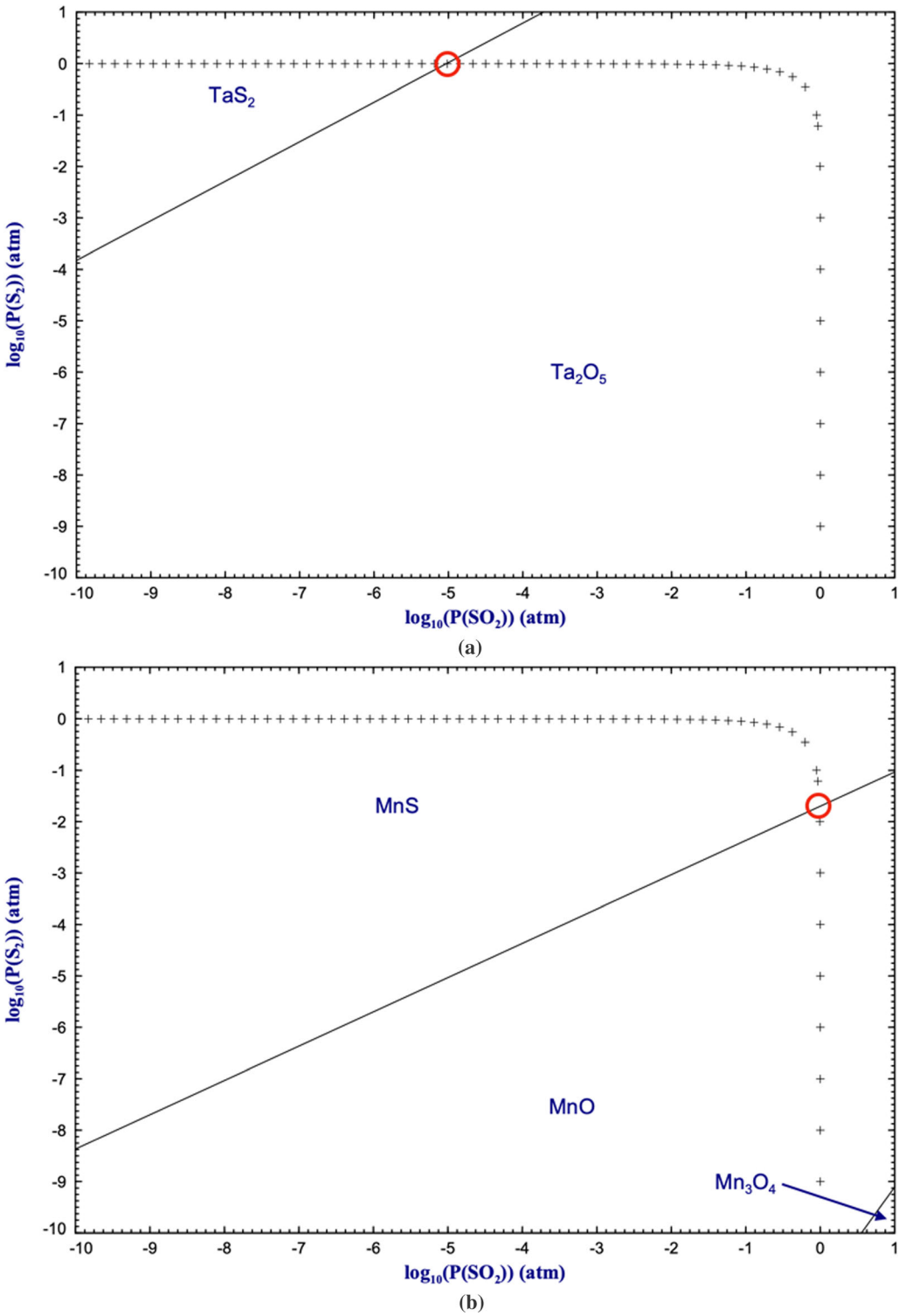

Fig. 3—Predominance diagrams of Ta–O–S and Mn–O–S at 1393 K, + line is the isobar at $p_{tot} = 1$atm (Color figure online).

reduction.[14] Residual contamination from silica was observed by the authors, altering the purity of the product. Spitczok *et al.* used ionic liquids dissolution (Lewis acidic solution of 34 mol pct dialkylimidazolium halide, 66 mol pct $AlCl_3$) to recover the tantalum-containing pellet and some residues of manganese oxide.[16] Katano *et al.* proposed a steam gasification process with sodium hydroxide (NaOH).[17] The mold resin is removed during the process, leaving a powdery silica that can be sieved out as tantalum pellets to keep their original shape. Fujita *et al.* used a two-step heat treatment to screen silica and tantalum powders.[18]

Pyrolysis processes (under Argon or Nitrogen) are also presented by Niu *et al.* and Chen *et al.* to remove the epoxy resin and recover the oil and gas as potential energy sources. Niu *et al.* then proposed a chloride metallurgy-based process to boil and selectively condense tantalum chloride.[19–21] Chen *et al.* used a process based on the LLE technology to extract tantalum oxide with hydrofluoric acid and extractant solutions (Alamine 336, MIBK, TBP).[22] Later, Chen *et al.* proposed a pyrolysis pre-treatment followed by hydrochloric acid leaching for manganese removal and chlorination of tantalum oxide for purity improvement.[23] Vacuum pyrolysis was also presented by Niu *et al.* as an alternative.[24]

Solvothermal treatment is shown by Sasaki *et al.*, where high-temperature and high-pressure solvents are used to separate the mold resin from capacitors.[25] Niu *et al.* presented a method for resin mold removal based on supercritical water.[26] Choi *et al.* developed a refining process including mechanical treatment, magnetic and density separation, refining electrolysis, and thermal oxidation to produce tantalum pentoxide with an overall recovery of 73 pct.[13] Agrawal *et al.* proposed two hydrometallurgical routes for tantalum oxide and metal recovery.[27,28]

From the above results, mold epoxy resin removal is crucial and challenging, as silica powder cannot be easily separated from tantalum oxide powder. The presence of impurities such as silver, graphite, and metallic alloys increases the complexity of the overall recycling process. Another important point highlighted by Padilla *et al.* is that the production of metallic tantalum, mainly as a powder, is primarily produced *via* the reduction of the potassium fluoride salt, not the oxide.[3] The relatively pure oxide produced during recycling must follow a similar K-salt route as if it were of lower purity. Finding a reduction process from oxide to metal to bypass the K-salt route is of interest for Ta recycling, as there is potentially no purification step required.

In the present process, the calcination step results in the formation of a ternary oxide $MnTa_2O_6$, by reaction of manganese oxide, tantalum oxide, and tantalum metal under air. This oxide is structurally akin to the end-members $MnNb_2O_6$, $FeNb_2O_6$ of the tantalite series and fits into the broader category of columbite supergroup mineralogy.[29,30] As described by Tarakina *et al.*, numerous phases exist in the ternary Mn–Ta–O[31,32] with a particularly large number of polymorphs of $MnTa_2O_6$.[33] Common XRD scans have been found to not be sufficient to fully distinguish these polymorphs or their degree of ordering.[34] Mössbauer spectroscopy is used instead to fully characterize the phases. Kinast *et al.* presented a study of multiple cation locations and ordering, using natural and heat-treated columbites under air and vacuum.[35] The particularity of $MnTa_2O_6$, as detailed by Turnock *et al.*, lies in its stability under varying oxygen partial pressures ($f_{O_2} \in [10^{-17}, 1]$ atm) and its large solid-solution domain.[36] The conventional approach of acid leaching, as investigated by Majima *et al.*, poses significant difficulties in dissolving these ternary oxides.[37] Their studies reveal that to dissolve AB_2O_6 oxides (where A is Mn or Fe, and B is Ta or Nb), highly acidic environments, rich in H^+ and F^- ions, are indispensable. These conditions highlight the complexities and inefficiencies inherent in the acid leaching process for A/B separation. In contrast, this paper aims to introduce a novel separation method and explore the promising capabilities of sulfide chemistry. This approach, based on the differential sulfide affinities of elements A and B, could present a more effective solution addressing the pressing need for new technologies in (Ta, Nb)/(Mn, Fe) separation.

Prior studies on sulfidation cover various chemistries and applications, from battery recycling[38] to metal refining[39] and rare earth separation.[40] Sulfidation and selective reduction of tungsten ore demonstrated a new potential route for metal production.[41] Ahmad *et al.* presented the sulfidation of ilmenite and chromite and noted the effects of sulfur (S_2), hydrogen sulfide (H_2S), and carbon (C) addition on the conversion rate and minimal required temperature. They also noted, as in the work presented herein, that the intra-grain porosity plays a key role in leveraging sulfidation limitations.[42] Selective sulfidation showed unprecedented results in physical and chemical separation allowing the treatment of ore and slag to recover elements of interest. Selective sulfidation in the term used herein, breaking an oxide to an oxide/sulfide mix, has been demonstrated by Han *et al. via* the selective sulfidation of lead smelter slag with sulfur, leading to the formation of an iron-rich zinc sulfide phase.[43] The selectivity *via* chemical separation can also be improved by sulfidation as in the case presented by Zhang *et al.* where two sulfide phases are produced post-sulfidation, and a selective hydrochloric acid leaching allows the separation of calcium sulfide and zinc sulfide.[44] Sulfidizing gases such as H_2S and CS_2 are less applicable for selective sulfidation and may involve carbon contamination for the latter.[45–49] Stinn *et al.* demonstrated that using gaseous elemental sulfur maximizes selectivity for individual sulfur products from mixed oxide feedstocks.[50]

The selective sulfidation step presented herein demonstrates the unique potential of this novel pyrometallurgy process. In the problem addressed here, hydrometallurgy paths rely on the dissolution and complexation of tantalum ions with fluorides anions. Selective sulfidation is instead based on the preferential affinity of each element for sulfur *vs* oxygen. In the case of tantalum and manganese, there is no literature suggesting the existence of ternary oxysulfides, sulfates, or sulfides. The

sulfidation conditions are found to form manganese sulfide and tantalum oxide from the ternary oxide. The solid-gas reaction is complex and the conversion from a ternary oxide to a mix oxide/sulfide involves several parameters: p_{S_2}/p_{SO_2}, temperature, carbon addition, particle size, inter- and intra- grain porosity, and initial feed purity. Some of these parameters are discussed herein, as limitations were observed during some of the experimental trials. Ta_2O_5 sulfidation instead is unselective and the conditions are chosen to maximize the conversion rate. A parallel to the Bedworth-Pilling ratio is proposed to discuss the observed limitations of sulfidation.[51]

II. METHODS

The capacitors processed herein were KEMET tantalum capacitors (T491A106K010AT, supplied by RS Americas, Supplier Part Number: 70095780). These capacitors are composed of tantalum (Ta), tantalum oxide (Ta_2O_5), manganese oxide (MnO_2), silver (Ag), carbon paste (C), alloy metallic frame (Zn, Cu, and Ni alloy), tin (Sn) for soldering, and an epoxy molded case with silica (SiO_2) fire retardant. The overall recycling process is described below and schematized in Figure 2.

A. *Pre-Treatment*

1. *Calcination*

The calcination step followed a similar procedure to the one described by Mineta *et al.*[14] Per batch of 6g (approximatively 200 units per batch), the capacitors were loaded on an alumina boat (Advalue Technology, SKU AL-5064, 100 mm length, 45 mm width, 19 mm height), the latter being disposed in the hot zone (127 mm hot zone length) of a horizontal furnace (CM Rapid Temp Furnace Bloomfield NJ) in a quartz tube (63.5 mm OD, Technical Glass product). Under air, the temperature was raised to 1150 K at a rate of 40 K/min and held for two hours. The furnace was then left to cool down naturally. Silica fiber refractory blanket was fitted on both side of the quartz tube next to the hot zone to limit thermal convection of air and keep the temperature homogenous. The calcination happened under a fume hood.

2. *Sonication and 40# mesh sieving*

Each batch of calcined tantalum capacitors was added to a glass beaker filled with deionized water (around 200 mL). The sonication allowed the density separation of silica floating in water, while the heavier components sank. After sonication for 15 minutes, the content of the beaker was sieved at a 40# mesh (425 μm maximum particle size, Hogentogler, SKU 5203, Stainless Frame—Stainless Cloth, No. 40), allowing the silica and small particles to pass through, while the large particles (containing the tantalum pellets) were collected on the mesh. The latter were again placed in the glass beaker and deionized water was added a second time. Several sonication and wet sieving steps were required until the water was fully transparent during sonication meaning that practically all the silica has been removed. The recovered phase was then relatively free of silica. The silica and other small particles could have been recovered from the deionized water. The large parts consisting mostly of either the tantalum-containing pellets or the alloy metallic frames and films were dried for several hours in a vacuum oven at 473 K.

3. *Electrostatic separation, automatic crusher, and sieving*

The recovered material was placed on a quartz plate to remove by hand any large silica particles potentially left. The shiny metallic films were removed by electrostatic separation as they stayed stuck on the quartz plate. By putting and removing the material from a quartz plate 15 to 20 times, all the remaining metallic thin films were removed. The particles were then crushed by batch of 40 g in a Rocklabs Benchtop Ring Mill (Type BTRM, Model 1A-BT) for 30 seconds. The metallic leads mainly deformed, while the sintered blocks broke into a fine powder. The mix was then sieved through a 70# mesh (210 μm maximum particle size) and a 325# mesh (45 μm maximum particle size). Most of the metallic leads stayed above the 70# mesh and the product of interest fell through the 70# mesh and was further passed through a 325# mesh for sulfidation. Most of the remaining impurities such as small pieces of metallic leads could not pass through the 325# mesh.

B. *Selective Sulfidation*

1. *Thermodynamic of sulfidation*

The pre-sulfidation treatment detailed above separated the epoxy mold, carbon, silica, metallic alloy frames, tin, and silver beads from the tantalum-containing phase $MnTa_2O_6$. The three major elements remaining were tantalum, manganese, and oxygen. Impurities such as silicon (Si), silver (Ag), nickel (Ni), zinc (Zn), tin (Sn), and copper (Cu) may have been present but will not be considered in the thermodynamic analysis. A ternary oxide $MnTa_2O_6$ was formed during the high-temperature calcination treatment. The quaternary Ta–Mn–O–S has not been studied in the literature. However, this ternary, among others (AB_2O_6, A = Mn, Fe; B = Ta, Nb), has been studied by Turnock *et al.* such that the conditions of thermodynamic stability of this phase can be found.[29,36,52,53] β-Ta_2O_5 and Mn_3O_4 were the two thermodynamic binary stable phases in these calcinating conditions (P_{O_2} = 0.21 atm, T = 1150 K).

Figure 3 shows the S_2-SO_2 predominance diagrams of Ta–O–S and Mn–O–S at a temperature of 1393 K (data from FactSage 8.0, FactPS database, FactSage TM). Following the isobars at 1 atm ($p_{tot} = p_{SO_2} + p_{S_2} = 1$ atm) on these systems, Ta_2O_5 is expected to convert into TaS_2 for $p_{S_2}/p_{SO_2} = 10^5$ (red circle), while Mn_3O_4 reduces to MnO in these conditions. Instead, MnO sulfidation is expected for

$p_{S_2}/p_{SO_2} = 10^{-2}$. This suggests a wide range of $p_{S_2}/p_{SO_2} \in [10^{-2}, 10^{5}]$ for the selective sulfidation of MnO into MnS in the presence of Ta_2O_5.

Gulyaeva *et al.* reported thermodynamic values for temperatures between 273 K and 1273 K for the orthorhombic ternary oxide $MnTa_2O_6$ synthesized from a mixture of MnO and Ta_2O_5.[54] Implementing their values for such ternary compound into calculation did not reveal a range of conditions to break this ternary into Ta_2O_5 and MnS, and therefore, such compound was not included further. Additionally, accurate measurements of standard enthalpy and entropy of formation of $MnTa_2O_6$ were not found in the literature. The anticipated selective sulfidation reaction is described by Equation [1].

$$2MnTa_2O_{6(s)} + \frac{3}{2}S_{2(g)} \rightarrow 2MnS_{(s)} + 2Ta_2O_{5(s)} + SO_{2(g)} \quad [1]$$

2. *Sulfidation experiment*

The sulfidation furnace used herein was similar in design to the one described in Stinn *et al.*[50] Three machinable alumina trays (50 mm OD, 47 mm ID, 25 mm height, 1.2 mm opening size, Cotronics) were custom-made. After machining, the crucibles were sonicated in acetone and dried in a vacuum oven for several hours. 100 g of sulfur powder (99.5 pct sublimed, Acros organics, CAS 7704-34-9) were melted and cooled down in a quartz crucible (25 mm OD, 150 mm height, Technical Glass Product), then loaded at the bottom of the furnace. 5 wt pct carbon powder (Glassy carbon, 99.95 pct purity, particle size between 2 to 12 μm, Aldrich) were homogeneously added to the mix oxide prior sulfidation to leverage the ratio p_{S_2}/p_{SO_2} as carbon reacts with S_2 and SO_2 to form carbon disulfide (CS_2), carbon monoxide (CO), and carbon dioxide (CO_2). The initial powder size is below 325 mesh, and the bed thickness per tray did not exceed 10 mm. Under 2400 sccm (0.04 L·s^{-1}) of Ultra High-Purity Argon flow (UHP Ar, less than 10 ppm O_2, AirGas) in an alumina tube, the temperature was raised from room temperature to 1393 K at 3 K per minute, then hold at the targeted temperature for 60 minutes and then brought down to room temperature at − 3 K per minute. The temperature inside the furnace was measured with a type K thermocouple protected by an alumina sheet in contact with the base of the bottom tray. The sulfur crucible was raised by 5 mm increments every 5 minutes during the 60 minutes at targeted temperature. The pressure in the reactor did not exceed 1 atm.

3. *Approximation of the p_{S_2} and p_{SO_2} values*

For an experiment of 60 minutes, boiling 100 g of sulfur (1.56 mol of S_2 total) led to 0.016 mol of S_2 gas per minute, while 2400 sccm (0.04 L·s^{-1}) of argon is equivalent to 0.097 mol of inert gas per minute, leading to the partial pressure of S_2, $p_{S_2} = 0.14$ atm, considering only these two gas species present at the entrance of the bottom tray. The partial pressure of SO_2 at the outlet of the tube furnace is measured by a Multiple Gas Analyzer (SO_2, CO, CO_2, H_2S, and O_2 quantification, Model IR-208, Infrared Industries).

C. *Nitric Acid Leaching*

1. *Reactivity of transition metal sulfides in nitric acid solution*

Ta_2O_5 and MnS were the two major phases expected post-sulfidation. While Ta_2O_5 is insoluble in nitric acid, MnS reacts vividly following Eq. [2] to form manganese sulfate ($MnSO_4$) highly soluble in water. Figure 4 shows the Pourbaix diagram for tantalum and manganese (FactSage 8.0, FactPS database) demonstrating the selectivity of the leaching step. The reaction was driven to completion by the constant removal of gaseous nitrogen dioxide (NO_2).

$$MnS_{(s)} + 8HNO_{3(sol)} \rightarrow MnSO_{4(sol)} + 4H_2O_{(sol)} + 8NO_{2(g)} \quad [2]$$

2. *Nitric acid leaching parameters*

The ternary oxide $MnTa_2O_6$ is insoluble in mild nitric acid hence only the trays with full conversion (absence of $MnTa_2O_6$) were sieved through a 100# mesh sieve (149 μm maximum particle size) then added to a 343 K 1M HNO_3 solution and stirred with a magnetic agitator at 200 rpm for 480 minutes. 100 mL of solution was used per gram of sample, leading to a concentration of HNO_3 at least five times superior to the stoichiometric concentration of MnS. The solution was then passed through a Büchner funnel equipped with a 1 μm filter paper. The filter paper was left to dry in a vacuum oven at 473 K for several hours. The deposited powder, Ta_2O_5, was then scrapped off the paper.

D. *Ta_2O_5 Sulfidation*

1. *Thermodynamic of sulfidation*

Post-acid leaching, the expected remaining phase was Ta_2O_5. The S_2–SO_2 predominance diagrams of Ta–O–S at a temperature of 1573 K are similar to the one at 1373 K (data from FactSage 8.0, FactPS database, FactSage TM). Following the isobar, Ta_2O_5 is again expected to convert into TaS_2 for a ratio $p_{S_2}/p_{SO_2} = 10^5$ (red circle in Figure 3). It is of interest to highlight the low thermal sensibility of the thermodynamic of sulfidation for the Ta_2O_5–TaS_2 system. The effect of impurities in the Ta_2O_5 phase or in other physical particles is unknown and not discussed herein.

2. *Sulfidation experiment*

A custom-made graphite tray (Graphite Store, 50 mm OD, 47 mm ID, 25 mm height, 1.2 mm opening size) was used as a crucible. After machining, the crucible was sonicated in acetone and dried in a vacuum oven for several hours. 100 g of sulfur powder (99.5 pct sublimed,

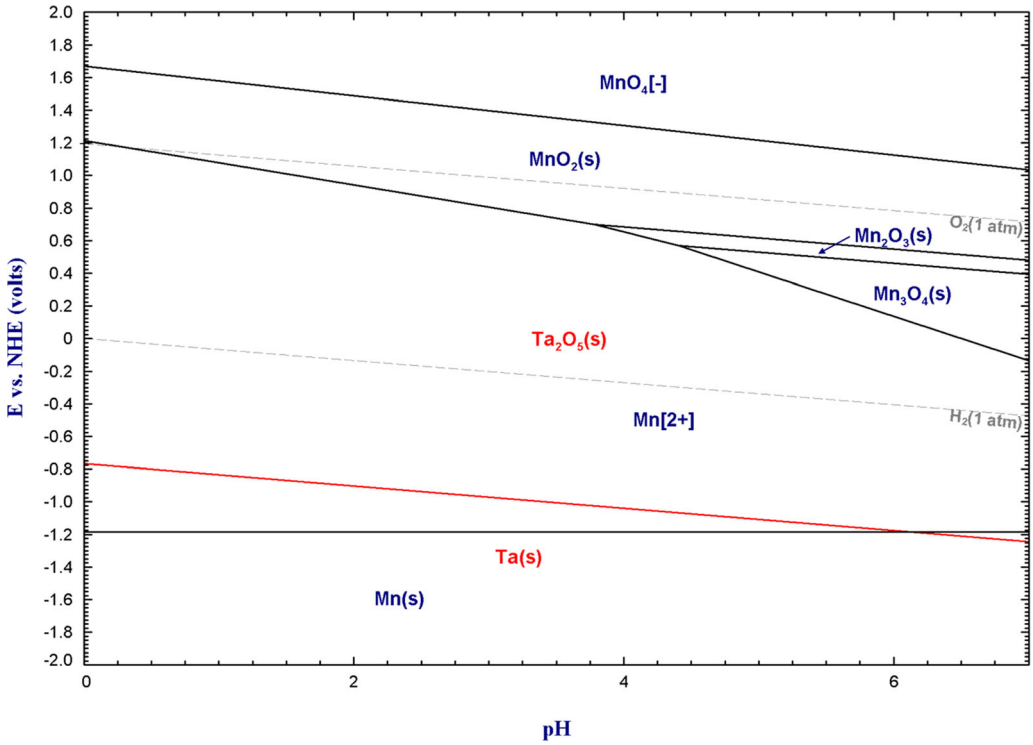

Fig. 4—Pourbaix diagram for tantalum (in red) and manganese (in black) at 343K in acidic media (pH < 7), total ion concentration 2 mol L^{-1}, Mn/Ta ratio = 1 (Color figure online).

Acros organics, CAS 7704-34-9) were melted and cooled down in a quartz crucible, then loaded at the bottom of the furnace. The initial powder size was below 325 mesh, and the bed thickness did not exceed 10 mm. Under 2400 sccm (0.04 $L{\cdot}s^{-1}$) of Ultra High-Purity Argon flow (UHP Ar, less than 10 ppm O_2, AirGas) in an alumina tube, the temperature was raised from room temperature to 1553 K at 3 K per minute, then held at the targeted temperature for 120 minutes. The sulfur crucible was raised by 5 mm every 5 minutes during the first 60 minutes at targeted temperature. After the 120 minutes at targeted temperature, the furnace cooled down to room temperature at − 3 K per minute. The pressure in the reactor did not exceed 1 atm. As shown later, two consecutive sulfidations in these conditions were necessary to fully sulfidize Ta_2O_5. Between both sulfidations, the powder was passed through a 325# sieve in a fume hood.

E. *Electro-Reduction*

1. *Thermal imaging furnace*

A container-less thermal imaging furnace (High Temperature Xenon Lamp furnace, Model TX-12000-I) was employed. Figure 5 shows a schematic of the furnace, and the sample was brought and maintained at temperature with four 3 kW xenon lamps focused with semi-spherical mirrors (not shown on Figure 5) on an approximative 1 cm^3 hot zone. The furnace has a controlled atmosphere in a 50 mm O.D. custom-made quartz tube (not shown) surrounding the set presented in Figure 5. The sample was prepared in a similar fashion as the ones presented in previous work[41,55]: the powders were mixed in a glove box (H_2O level < 10 ppm) and compacted with an isostatic press (30 000 psi) into a rod of 5 g, about 10 mm in diameter. The electrolyte sample was then held in the xenon lamps focus *via* a top shaft and the bottom tip of the sample was molten by capillarity allowing a "container-less" experiment. The electrodes, described in the next paragraph, were brought to contact with the electrolyte *via* an alumina bottom shaft. The furnace tube was evacuated to a pressure of 10^{-3} atm and re-purged with UHP Ar three times. 200 sccm (0.003 $L{\cdot}s^{-1}$) of UHP Ar were then flowed continuously during the electrolysis experiment.

2. *Electrolyte composition and electrodes*

The electrolyte sample was composed at 90 wt pct of BaS–La_2S_3 supporting electrolyte[39] (62–38 wt pct respectively) mixed with 10 wt pct TaS_2 obtained from the process presented above. Figure 6 represents the decomposition potential of BaS, La_2S_3, and TaS_2 in function of temperature (data from FactSage 8.0, FactPS database). BaS and La_2S_3 have a higher standard decomposition potential than TaS_2 in the temperature range 1000 °C to 2000 °C, suggesting the latter can be selectively electro-reduced to its metallic form by electrolysis. This specific electrolyte composition is fully liquid above 2000 K as determined by thermal analysis, and the standard decomposition voltage of pure TaS_2 at this temperature is around -0.35 V. The temperature could not be monitored during the electrolysis process. The cathode was a tungsten working electrode (W wire,

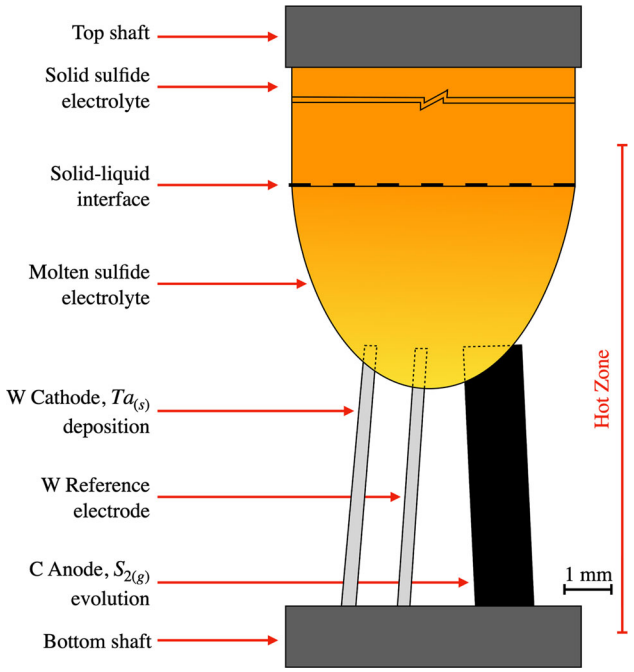

Fig. 5—Schematic of the container-less thermal imaging furnace containing the pendant droplet liquid electrolyte and the inserted probes for electrochemical experiments.

0.25 mm diameter, 99.9 pct purity, VWR), the reference electrode was a quasi-reference also made of tungsten (W wire, 0.25 mm diameter, 99.9 pct purity, VWR), and the anode was a custom-made graphite counter electrode (EDM quality graphite, around 1 mm diameter, Graphite Store).

3. *Electro-reduction experiment*

A Gamry Reference 3000 potentiostat (Gamry Instruments, 734 Louis Drive, Warminster, PA 18974) and a high-frequency data acquisition hardware (Dynamic Signal Analyzers, Data Translation, DT9837B) were used to conduct electrochemical measurements and separately measure the cell voltage. The sample was heated up above its melting point and the electrodes were then inserted. A fixed potential between the working and reference electrodes was applied for 2,000 sec (Chronoamperometry). The expected decomposition reactions at the electrodes are the following: at the cathode/working electrode: $Ta^{4+} + 4e^- \rightarrow Ta_{(s)}$; at the anode/counter electrode: $2S^{2-} \rightarrow S_{2(g)} + 4e^-$.

F. *Characterization*

Samples were analyzed by Induction-Coupled Plasma—Atomic Emission Spectroscopy (ICP-AES, Applied Technical Services, 1049 Triad Court, Marietta, GA 30062), LECO combustion (Applied Technical Services, 1049 Triad Court, Marietta, GA 30062), and X-Ray Diffraction (XRD, PANalytical X'Pert Pro XRPD, MIT MRL facilities, MA, 02139). Other elemental analysis was conducted with a Scanning Electron Microscope (SEM, JEOL JSM- 6610LV, JEOL Ltd.) equipped with an Energy Dispersive Spectroscopy

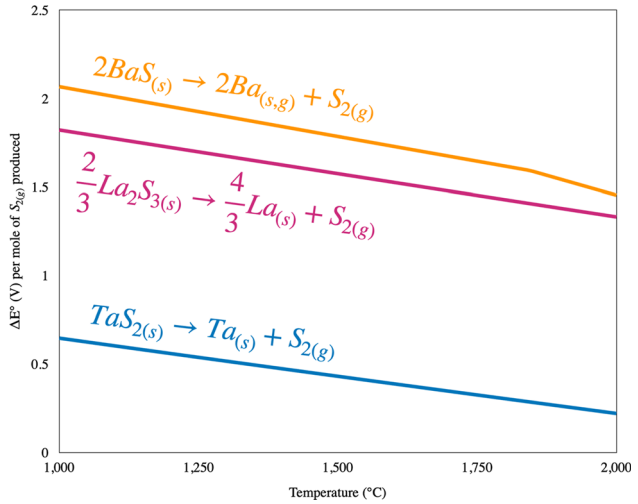

Fig. 6—Standard decomposition voltage of tantalum sulfide, lanthanum sulfide, and barium sulfide as a function of temperature.

(EDS, Sirius SD detector, SGX Sensor-tech Ltd.) detector. For the latter analytical method, all samples have been polished up to 0.25 μm with kerosene (Sigma Aldrich, reagent grade, low odor, CAS number 8008-20-6). Post-electrolysis, the electrolyte was mounted in epoxy, cross-sectioned, polished, and analyzed.

III. RESULTS AND DISCUSSION

A. *Pre-Treatment*

1. *Calcination*

The pre-treatment of the capacitors had a key role on the overall process, either in terms of purity or recovery of the end-product. As discussed by Mineta *et al.*,[14] the temperature control is essential as a set temperature below 973 K breaks the structure of the tantalum-containing pellet and lower drastically the recovery rate during sieving. Temperatures higher than 1173 K allow the formation of silica lumps with silver, reducing the purity of the recovered phase. Figure 7 presents pictures of capacitors before and after the calcination step. The orange/salmon color of the remaining silica was clearly visible. When the calcination step was incomplete, a black deposit was visible, and the silica powder did not crumble easily. In Figure 7, the large black particles are the tantalum pellets, and the white leads are the central metallic connector leads of the positive terminal. The average mass loss of 6.57 wt pct corresponded approximatively to the mass fraction of epoxy (excluding the silica) and carbon combustion in a capacitor, accounting for the oxidation of the metallic parts.

2. *Sonication and 40# mesh sieving*

The sonication allowed the flotation of the silica fine powder. However, it was noticed that part of the tantalum pellets would also break as the sonication time increased. Those small particles rich in Ta would be lost through the 40# mesh sieve, as well as any tantalum wire

contained within the pellet. The use of a finer mesh sieve would have necessitated longer sonication times, resulting in a trade-off with the recovery of the pellets as they are prone to breaking over time.

3. *Electrostatic separation, crushing, and sieving*

From the 7000 capacitors treated, the electrostatic separation allowed the removal of around a hundred of thin metallic films. A dozen of pieces containing silica chunks were eye-spotted and manually removed too. The crushing step produced a fine powder, some deformed metallic frames components, and small metallic impurities to a low extent. The fine powder was the main product of interest as it was mainly composed of $MnTa_2O_6$. It was obtained by sieving through a 325# mesh. Its atomic composition is presented in Table I, line 1, and presents a low concentration of impurities. A product of lower purity containing a larger proportion of metallic impurities was also obtained, the particle size was lower than 70# mesh but higher than 325# mesh: between 45 and 210 μm. Its composition is also presented in Table I, line 2. The large metallic frames could be sonicated to maximize the recovery of the fine powder; however, a higher metallic impurity concentration was also observed in the recovered powder. Its composition is presented in Table I, line 3.

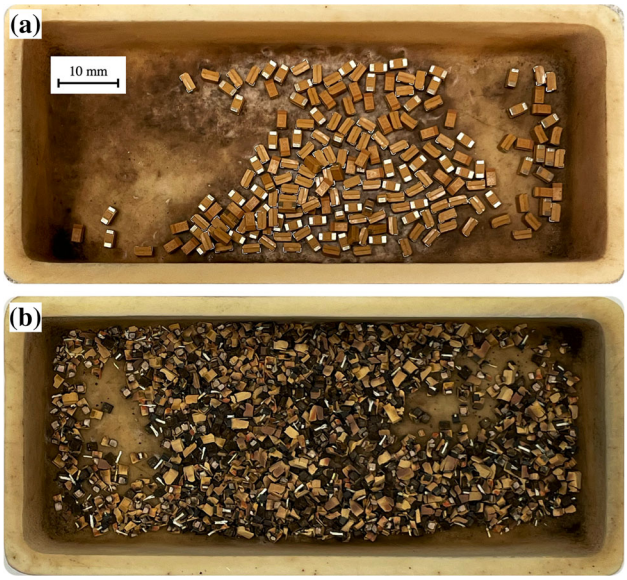

Fig. 7—Tantalum capacitors in an alumina boat (*a*) before; and (*b*) after calcination (Color figure online).

4. *Purity and optimization at large-scale*

Table I shows the elemental composition of different powder mix at different stages of the process. The column "other" is composed of the following elements that are not known to be part of tantalum capacitors by the authors: Al, Ca, Cr, Fe, K, Mg, Mo, Na, P, Ti, V, and Co. For all samples analyzed by ICP-AES, the major elements of the "other" column are Na, Ca, and Mg, contaminants that may arise from the water for sonication or during sample analysis.

Comparing lines 1, 2, and 3 indicates an increase in the content of certain metallic elements (Ag, Zn, Cu, Ni, and Sn), as discussed previously. The concentration of carbon and silica is low, emphasizing the proper implementation of the pre-treatment. An optimized set-up would greatly enhance the overall recovery of the process, especially the anodic tantalum wire not recovered herein. The physical separation between the pellet, the wire, the metallic case, and metallic leads should be achievable due to the relatively large size difference between the different entities.

B. *Selective Sulfidation*

1. *Observation and chemical analysis*

Figure 8 shows the three alumina trays loaded in the reactor before and after selective sulfidation, in addition with the thermal profile of the furnace. More than 60 g of surrogate were divided between each tray and represent more than 7,000 processed capacitors. Post-sulfidation, only the top tray was partly covered with a yellow deposit. Figure 9 presents macroscopic optical observation of a cross-section post-selective sulfidation of the bottom and top trays. The middle tray was found to be identical to the bottom tray. A homogeneous black color is characteristic of the full conversion of the bottom and middle trays, while the

Table I. Elemental Composition of the Powder at Different Stages of the Process, as Measured by LECO (* for C, S, and O) and ICP-AES Analysis, Values are in Wt Pct

Element	C*	S*	O*	Ag	Mn	Si	Zn	Cu	Ni	Sn	Other
Feed for Sulfidation	0.04	0.01	18.60	0.28	11.80	0.22	3.10	2.20	0.76	0.19	1.37
Particle Size $\in$ [45; 210] μm	0.05	0.01	22.00	1.20	11.00	0.27	3.70	7.40	2.70	0.22	1.60
Powder from Sonication of Metallic Frames	0.08	0.08	24.80	0.33	13.00	0.11	5.40	3.30	1.70	1.10	1.58
After Sulfidation, Bottom Tray	1.40	9.40	17.70	0.28	12.20	0.24	0.63	2.10	0.72	0.01	1.52
After Sulfidation, Middle Tray	1.20	9.60	17.40	0.34	11.30	0.19	0.27	2.10	0.73	0.03	1.97
After Sulfidation, Top Tray	3.30	4.40	20.50	0.33	10.80	0.22	2.30	2.00	0.70	0.06	1.49
After Acid Leaching of Sulfidized Bottom Tray	2.10	0.19	19.40	0.14	0.06	0.15	0.40	0.05	0.02	0.04	1.91
After Acid Leaching of Sulfidized Middle Tray	1.60	0.19	20.90	0.20	0.09	0.23	0.21	0.07	0.02	0.02	2.05
After Ta_2O_5 First Sulfidation	0.14	22.60	3.40	0.04	0.08	0.13	0.49	0.08	0.02	0.02	2.39
After Ta_2O_5 Second Sulfidation	0.80	25.20	1.20	0.05	0.12	0.07	0.53	0.09	0.02	0.03	2.67

The concentration of tantalum is too high to be quantified correctly by ICP-AES.

top tray presented a gradient of color, characteristic of partial conversion.[56] The alumina trays did not react with the feedstock or product, or the vaporized sulfur, as predicted by Stinn *et al.*[50]

Figure S1 (see electronic supplementary) presents the XRD analysis of the feed and products of sulfidation for the bottom and middle trays. Before sulfidation the main phase is orthorhombic $MnTa_2O_6$. The degree of ordering of $MnTa_2O_6$ is not discussed herein. In the work of Turnock on Mn–Ta oxides, the orthorhombic phase is the stable one.[36] The present $MnTa_2O_6$ phase is not found in product of the bottom and middle trays, and Ta_2O_5 and MnS are now the two main phases, some residual C (graphite) is also visible on the XRD. The selective sulfidation on the bottom and middle trays went to completion and is selective. The top tray materials, which XRD pattern is presented in Figure 10, still contained some $MnTa_2O_6$—the orthorhombic phase—in addition to Ta_2O_5, MnS, and unreacted graphite. Impurities and amorphous phases could not be quantified or identified from these XRD results.

Table I, lines 4, 5, and 6 present the elemental composition of each tray post-sulfidation. The concentration of sulfur in the bottom and middle trays was 9.40 and 9.60 wt pct, respectively, while the sulfur top tray content was 4.40 wt pct. The total Mn content was approximatively constant across the three trays, before and after sulfidation indicating a negligible vaporization of Mn at 1393 K. This is consistent with its presence in oxides or sulfides. The concentrations of Ag, Ni, and Cu were identical in every tray and invariant upon sulfidation. They were expected to form sulfides according to thermodynamic predictions.[50] The concentration of Si also remained constant through sulfidation though Si was expected to remain an oxide.[50] The content in Zn and Sn (resp. 3.10 and 0.19 wt pct in the feed) decreased significantly upon sulfidation, especially for the bottom and middle trays (0.63 and 0.27 wt pct, respectively, for Zn, 0.01 and 0.03 wt pct, respectively, for Sn). The yellow deposit on the trop tray, visible in Figure 8(c), was analyzed by EDS and consisted of ZnS particles, as expected from the high vapor pressure and low boiling points of zinc sulfide.[57] As the temperature at the top tray was lower than at the bottom and middle trays, a higher concentration of ZnS remained as solid in this tray, as shown in Table I, line 6. The C powder added for sulfidation is not totally consumed during the experiment. A lower temperature and lower conversion rate explained the higher concentration of carbon post-sulfidation in the top tray (3.30 wt pct) compared to the bottom and middle trays (1.40 and 1.20 wt pct, respectively).

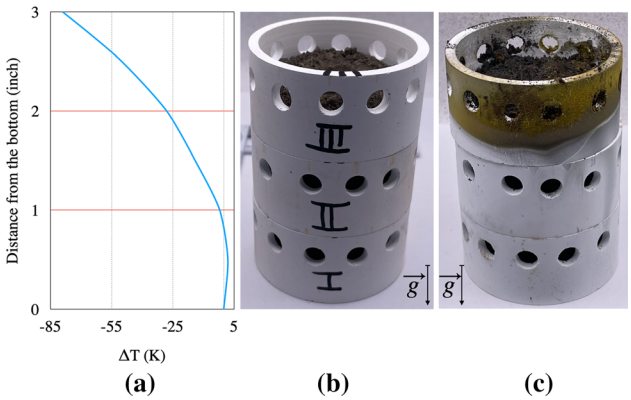

Fig. 8—(*a*) Thermal gradient in the furnace during sulfidation where the origin of the *y* axis is at the base of the lower tray and the reference temperature is the targeted temperature; (*b*) trays before sulfidation; (*c*) trays post-sulfidation.

The MnS, Ta_2O_5, and $MnTa_2O_6$ content for the trays post-sulfidation, presented in Table II, is calculated from the metal content presented in Table I for Mn, Ag, Zn, Cu, Ni, Sn, and Si and the following assumptions inherited from our observations:

(1) the metallic elements were present in the following oxides and sulfides phases: MnS, Ag_2S, ZnS, Cu_2S, Ni_2S_3, SnS, SiO_2, Ta_2O_5, $MnTa_2O_6$ meaning that the manganese can only be present as MnS or $MnTa_2O_6$ and the oxygen distributes only between SiO_2, Ta_2O_5, and $MnTa_2O_6$.
(2) $MnTa_2O_6$ phase is fully decomposed in the bottom and middle trays post-sulfidation.
(3) Column "Other" in Table II is ignored.

Table II. Compound Concentrations (in Wt Pct) Post-Sulfidation and Post-Nitric Acid Based on Assumptions Detailed in the Relevant Section of the Article

Phase	Bottom Tray Post-Sulfidation	Middle Tray Post-Sulfidation	Top Tray Post-Sulfidation	Bottom Tray Post-Nitric Acid	Middle Tray Post-Nitric Acid
Carbon	1.14	1.01	2.63	1.92	1.37
MnS	15.74	15.01	3.60	0.09	0.12
Ag_2S	0.26	0.33	0.30	0.15	0.20
ZnS	0.77	0.34	2.74	0.54	0.27
Cu_2S	2.14	2.21	2.00	0.06	0.07
Ni_2S_3	1.07	1.11	1.02	0.03	0.03
SnS	0.01	0.03	0.06	0.05	0.02
SiO_2	0.42	0.34	0.38	0.29	0.42
Ta_2O_5	78.45	79.62	28.03	96.88	97.50
$MnTa_2O_6$	—	—	59.24	—	—

Based on the above assumption, a simple way to define a conversion ratio was on the amount of manganese sulfide MnS produced. A full conversion corresponds to around 15.38 wt pct MnS (average of the bottom and middle trays). The partial conversion of the top tray can then be calculated to be 23 pct from the amount of MnS produced: 3.60 wt pct.

The ratio p_{S_2}/p_{SO_2} for such experiment was calculated from the gas analyzer data, argon flow, and partial pressure of sulfur. An approximative total of 0.023 mol of CO, 0.012 mol of CO_2, 0.006 mol of H_2S, and 0.001 mol of SO_2 were measured by the gas analyzer over the hour-long sulfidation. During sulfidation, 5.82 mol of Ar and 1.56 mol of S_2 were flowed. Considering the low proportion of SO_2 and H_2S, the partial pressure of sulfur was considered constant and the partial pressure of CS_2 was not considered. The ratio p_{S_2}/p_{SO_2} was then around 10^3, sufficient for selective sulfidation of Mn according to Figure 3.

2. *Characteristics and limitations of selective sulfidation*

Figure 11 shows an SEM/BEC observation post-selective sulfidation of a representative particle from the bottom and middle trays materials. The decomposition of a single ternary oxide particle generated micrometric-scale particles of Ta_2O_5 particles (light phase) embedded into MnS (dark phase). A similar partitioning was observed during the sulfidation and selective reduction of tungstate mineral phases.[41] The morphology of the product was advantageous for acid leaching, as the surface area of MnS increased and the Ta_2O_5 particles were large enough (few μm) to be filtered.

The results presented herein do not allow complete explanation of the limited conversion observed for the top tray. SEM/BEC analysis showed that most of the particles were unreacted, while few particles presented a thin outer layer of sulfide, and fewer fully converted. From the physical gradient presented in Figure 9, it can be hypothesized that the conversion rate was higher at the bottom than at the top of the tray. The ratio of loaded sulfur to the stoichiometrically required amount of sulfur to form MnS is above 20, and therefore, it is not expected that the amount of sulfur was a limiting factor for the top tray conversion. The following facts potentially explain the observed limitations:

1. Lower temperature—the gradient of temperature inside the furnace, shown in Figure 8, led to a local temperature for the top tray insufficient for the ternary oxide conversion. Either thermodynamic or kinetic limitations may be at play here.
2. SO_2 abundance—sulfur flows first through the bottom tray, then the middle tray, and lastly through the top tray. The bottom and middle trays are reacting first, scrubbing some S_2 and generating some SO_2. This may drive the p_{S_2}/p_{SO_2} ratio down and prevents the sulfidation reaction of the top tray. Once again, either thermodynamic or kinetic limitations may impede the reaction rate.

3. *Tantalum-containing sulfide and the role of p_{S_2}/p_{SO_2}*

Not observed in the experimental conditions reported herein, a tantalum-rich sulfide phase was observed in certain experimental conditions. The exact composition of the phase, its crystal structure, or domain of stability is unknown to the authors even after an extended literature research. XRD analysis presented this phase as TaS_2, and SEM/EDS analysis suggested a high solubility (> 1 wt pct Mn) of Mn in this phase. Si had no solubility in this sulfide phase. Nitric, hydrochloric, and sulfuric acids at 1M and room temperature did not dissolve this sulfide phase. This phase was found in similar experimental conditions as described above, but only when a smaller quantity of ternary oxide powder was processed (single identical alumina tray with 5-10 g of feed). In those conditions, the sulfide phase was visible on the XRD scan. The experiment presented herein, instead with a larger initial mass of material, demonstrated a full selective sulfidation of manganese for the bottom and middle tray, while the top tray did not go to completion, for reasons proposed above. It is supposed that a sufficient proportion of SO_2 was generated through the entire sulfidation time, thanks to the large quantity of reactants, maintaining the p_{S_2}/p_{SO_2} ratio in the range for selective sulfidation shown in Figure 3. With a smaller batch, the SO_2 produced may not have been sufficient to maintain the p_{S_2}/p_{SO_2} ratio in the range of selectivity, leading to the co-sulfidation of manganese and tantalum into MnS and TaS_2. Practically, the p_{S_2}/p_{SO_2} ratio could be tuned by either the bleeding of SO_2, or O_2 during sulfidation. For a similar—small—quantity of loaded sample and identical experimental conditions leading to non-selective sulfidation, a higher temperature ($1393\ K < T < 1553\ K$) led to more intense XRD peaks for the TaS_2 phase. Further work on the solubility of Mn in TaS_2, possible ternary sulfides Ta-Mn-S, and quaternary oxysulfides Ta-Mn-S-O is required to better explain this result.

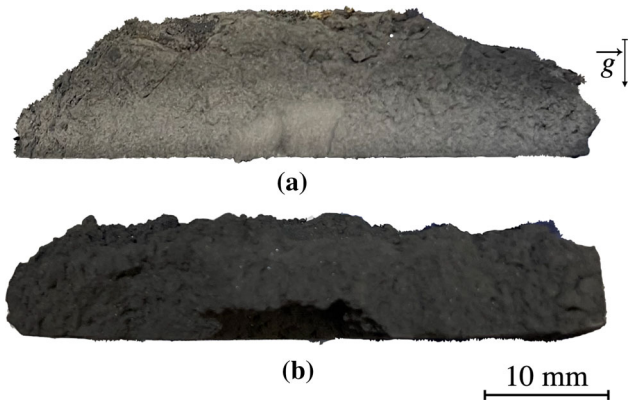

Fig. 9—Fractured and cross-sectional optical views of (*a*) the top tray; (*b*) the bottom tray (middle tray is similar) (Color figure online).

C. *Manganese Sulfide Removal by Acid Leaching*

The bottom and middle trays from selective sulfidation were fully converted into a mix of manganese sulfide and tantalum oxide; no ternary oxide $MnTa_2O_6$ was observed by XRD. As expected from Eq. [2], manganese sulfide reacted with the nitric acid solution to form a sulfate, readily soluble in water.[58] Figure S2 (see electronic supplementary) presents the XRD spectrum of the resulting powder after the acid leaching. The single-phase remaining is the low-temperature orthorhombic tantalum oxide Ta_2O_5.[36,59] Figure 12 shows an SEM/BEC image of Ta_2O_5 from the bottom tray; the particle size is below 25 μm indicating limited coarsening of Ta_2O_5 grains during sulfidation. It is essential to notice the porosity of the Ta_2O_5 aggregates, which is important to support a subsequent sulfidation to TaS_2.

Table I, lines 7 and 8 present the elemental composition of materials from the bottom and middle trays after nitric acid leaching. Table II presents the final purity of the Ta_2O_5 phase. The main impurity is the unreacted graphite (1.92 and 1.37 wt pct for the bottom and middle tray respectively) followed by the zinc sulfide in the bottom tray (0.54 wt pct) and the silica in the middle tray (0.42 wt pct). The content of metallic alloy impurities such as Cu and Ni lowered. The sulfidation step allowed the formation of transition metal sulfides (CuS, NiS), which are also reactive in nitric acid solutions forming transition metal sulfates ($CuSO_4$, $NiSO_4$), highly soluble (> 100 g/L) in aqueous solutions. Zn and Ag concentrations were also slightly decreased. The concentration in silica (SiO_2) may also be decreased due to the relative solubility of silica in mild acid media.[60] The excess carbon particles from the sulfidation may have been partially removed by floatation during the acid treatment. The sulfidation and solubilization were observed to be kinetically limited; several trials not presented herein showed an increase in impurity content for lower leaching time.

D. *Ta_2O_5 Sulfidation*

1. *Parameters for Ta_2O_5 sulfidation*

Thermodynamically, the critical ratio $p_{S_2}/p_{SO_2} = 10^5$ for the sulfidation of Ta_2O_5 into TaS_2 is almost independent on the sulfidation temperature. The higher temperature for the Ta_2O_5 sulfidation was expected to increase the kinetics of reaction and lead to completion in a shorter time, as observed by Stinn *et al.*[50] The effect of temperature on other gas-solid reactions such as the formation of CS_2 is not discussed herein. It should also be noted that the partial pressure of sulfur (p_{S_2}) during the selective sulfidation (1393 K) and Ta_2O_5 sulfidation (1573 K) is similar, as described in II.c. In those conditions, and to thermodynamically drive the sulfidation reaction forward, the main leverage was therefore the partial pressure of SO_2. During the selective sulfidation of the mixed oxides, alumina trays and graphite powder were used to balance the ratio p_{S_2}/p_{SO_2} between 10^{-2} and 10^5. Instead, a graphite tray was used during the Ta_2O_5 sulfidation to drastically lower the partial pressure of SO_2, leading to a more reducing environment. Increasing both the temperature and the p_{S_2}/p_{SO_2} allowed the formation of TaS_2 in two consecutive sulfidation runs.

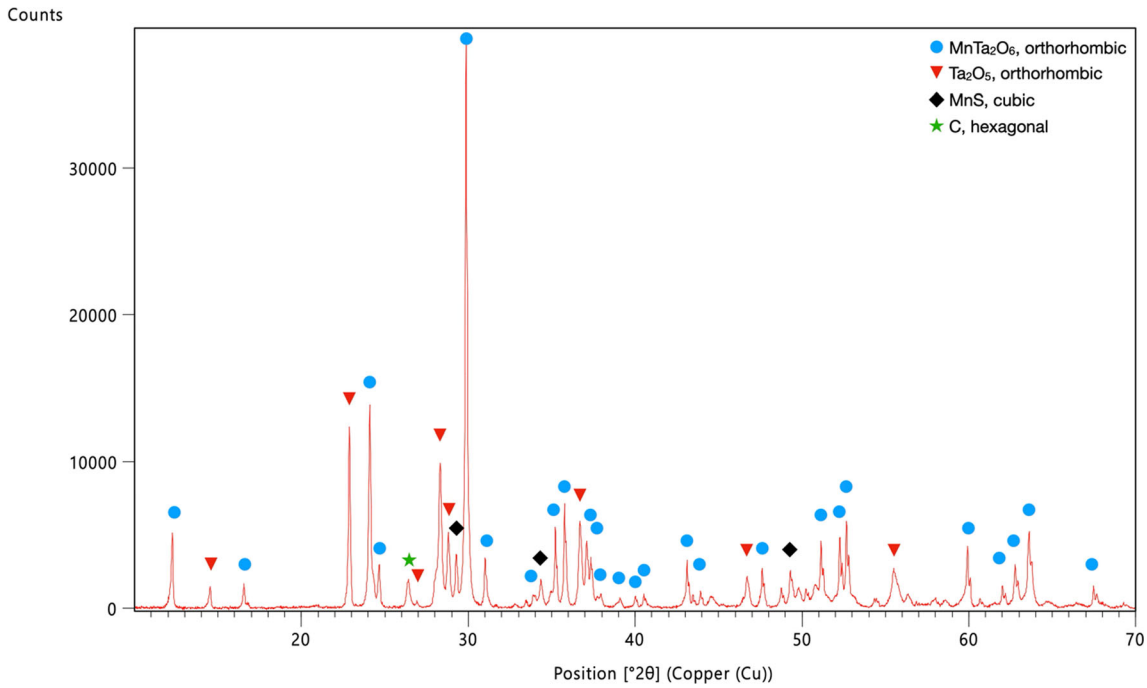

Fig. 10—XRD scan top tray post-selective sulfidation, presenting partially reacted materials.

2. *Limitations in the Ta_2O_5 sulfidation*

It was observed that a single sulfidation run was insufficient to fully convert Ta_2O_5 into TaS_2 in the present experimental set-up. Two consecutive sulfidations were then required to reach a high level of conversion. Figure S3 (see electronic supplementary) presents the XRD spectra of the powder after the first and the second sulfidation. The absence of oxysulfides is noticeable, instead the phase observed by XRD after second sulfidation is TaS_2. ICP-AES and LECO analysis, presented in Table I, line 9 and line 10, confirmed the conversion of the oxide to a sulfide observed by XRD.

From the cross-section analysis, no limitation for sulfur transport through the bed (< 10 mm) was observed. Inter-grain limitation was not observed neither as the bed was not pre-compacted nor densified during sulfidation. Figures 13(a) and (c) represent two SEM/BEC images of a single grain after the first and second runs. Figures 13(b) and (d) present an EDS ratio map of the weight fraction of sulfur over the total anionic weight fraction ([S]/([S] + [O])). Two phases are observable, Ta_2O_5 in dark blue, and TaS_2 in yellow. The oxide–sulfide interface is sharp, with limited solubility of oxygen is the sulfide and sulfur in the oxide phases, and confirming the absence of oxysulfides.

The large initial porosity of the Ta_2O_5 particles, resulting from the selective sulfidation and acid leaching, seemed to favor intra-grain sulfidation, thanks to a high reaction surface to volume ratio. In non-porous regions of the materials, the remaining oxide fraction was surrounded by a sulfide layer. This type of limitation has been observed in previous work on scheelite sulfidation.[41] Identifying a sulfidation reaction model is not obvious from those findings. As stated by Ishida *et al.*,[61] solid-gas reactions at such scale often cannot be completely described either by the unreacted-core shrinking model or by the homogeneous model.[62,63] Herein, perhaps a hybrid model of these two is needed. However, further work is warranted to understand whether the mass transport of sulfur to the oxide–sulfide interface, or the chemical reaction controls the overall reaction rate.

The Pilling–Bedworth (P–B) ratio, presented in Eq. [3], has been stated originally to differentiate metals forming a passive oxide layer (P–B ratio $\in$ [1;2]) and those who cannot (P–B ratio < 1; and P–B ratio > 2) under dry air. This P–B ratio is defined as the ratio of the unit cell volume of the metal oxide (V_{oxide}) to the unit cell volume of the corresponding metal (V_{metal}). For P–B ratio $\in$ [1;2], the oxide layer formed is dense and further limits the reaction of the metal with oxygen due to the slow diffusion of oxygen through the oxide layer. In the case of the Ta_2O_5 sulfidation, the sulfur diffusion through the sulfide phase to the oxide phase may be the cause of the limited sulfidation kinetics observed herein. To validate this hypothesis, a modified P–B ratio formula is given below (Equation 3), for an oxide/sulfide interface as relevant herein. Ta_2O_5 has an orthorhombic structure and a unit cell volume of approximatively 178 Å[3,64] for an equivalent Ta_4O_{10} cell. The 2H-TaS_2 possesses a hexagonal crystal structure and a unit cell volume of approximatively 115 Å[3,65,66] for an equivalent Ta_2S_4 cell.

$$R_{PB} = \frac{V_{oxide}}{n \times V_{metal}} \leftrightarrow \frac{V_{sulfide}}{m \times V_{oxide}} = 1.29 \qquad [3]$$

V_X is the volume of the unit cell volume for phase X(oxide, sulfide, or metal), n is the number of atoms of metal per oxide molecule, and m is the number of atoms of metal in the sulfide per atoms of metal in the oxide (herein ½ for Ta_2O_5 vs TaS_2). For such modified P–B ratio, it is assumed that the formation of sulfide layer "passivates" and protect the core oxide from further sulfidation. The limitations would therefore be linked to the diffusion of sulfur through the newly formed sulfide layer. This hypothesis seems also confirmed by the visually dense phase of TaS_2 and the absence of rough interface between the oxide and sulfide phases.

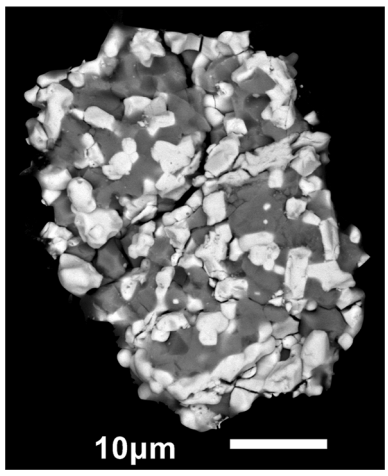

Fig. 11—SEM/BEC image of representative materials from the bottom tray after sulfidation. The light phase is Ta_2O_5, the dark phase is MnS.

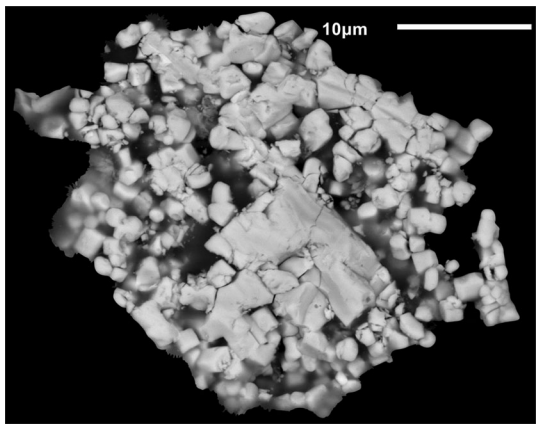

Fig. 12—SEM-BEC observation of representative materials from the bottom tray after sulfidation and nitric acid treatment. The blurry areas come from the epoxy resin mounting for analysis.

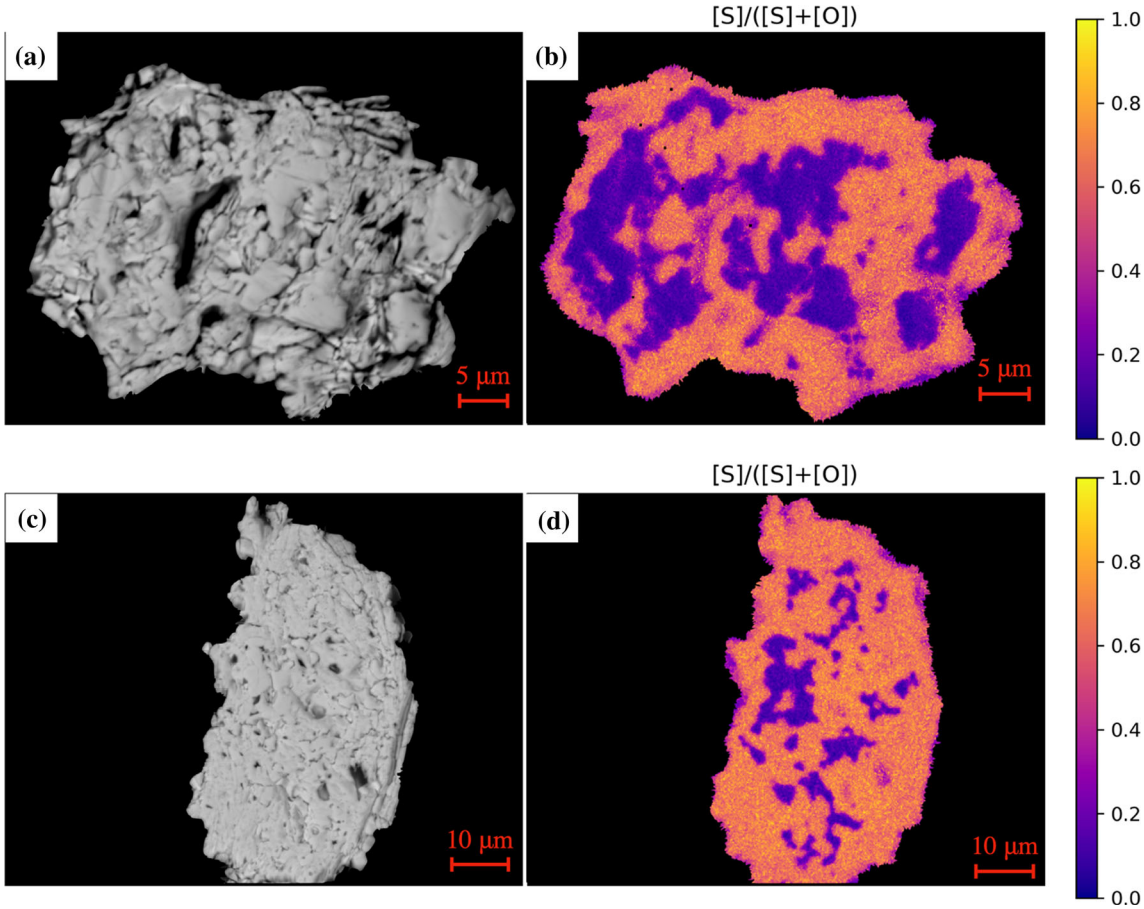

Fig. 13—SEM BEC cross-sectional observation of Ta_2O_5/TaS_2 particles (left), and the corresponding EDS maps (right) with the color intensity showing the ratio [S]/([S] + [O]) (*a* and *b*) after first sulfidation; (*c* and *d*) after second sulfidation (Color figure online).

E. *Electro-reduction*

Figure 14 shows the electrolysis assembly during a chronoamperometry experiment (Figure 14(a)) and the corresponding electrochemical signals (Figure 14(b)). The total cell voltage was large compared to the minimum thermodynamic decomposition potential (see Figure 6), mainly due to the set-up consisting of thin W wires (~ 0.25 Ohms) and a graphite anode pressed into a molybdenum cylindrical support (~ 6 to 7 Ohms) leading to a large ohmic drop. Figure 14(c) shows a SEM and BEC images of a horizontal cross section of the solidified electrolyte after the experiment. Figure 14(d) shows the map of EDS point analysis for elemental sulfur distribution. Two regions are observable; Ta metal in dark blue, and the sulfide electrolyte in purple, partially depleted in tantalum. The metallic tantalum was not deposited on the cathode for reasons not investigated herein. Recovering the tantalum metal produced was difficult in such set-up due to the small particle size and large dispersion throughout the melt. In a more conventional furnace, it could be expected that the tantalum particles sink due to their high density. The recovery methods, including physical separation (crushing and sieving or centrifugation[67]) or froth flotation,[68] are not discussed herein.

F. *Practical Limitations for Quantitative Study*

The proposed process is a novel approach for the recovery of tantalum oxide or tantalum metal from tantalum capacitors, with a focus on establishing the purity of tantalum oxide, post-nitric acid treatment. The selective breakdown of $MnTa_2O_6$ which is crystallographically similar to natural mangano-tantalite ore suggests a potential pathway for ore refining. Up to the electro-reduction of TaS_2, no major new reactor technologies are needed. However, a quantitative study of the recovery rate has not been conducted, for the following reasons:

1. The pre-treatment is not yet optimized in terms of energy consumption or tantalum recovery. A custom-designed sieving apparatus would significantly enhance the retrieval of tantalum-containing components (*e.g.*, electrode materials) and facilitate the removal of silica and other metallic impurities.
2. The selective sulfidation could be implemented as a continuous process, using $MnTa_2O_6$ and S_2 as inputs, yielding MnS, Ta_2O_5, and SO_2. The process temperature, below 1473 K, poses no technological challenges, and the reducing environment (S_2, SO_2) has minimal impact on refractory oxides.

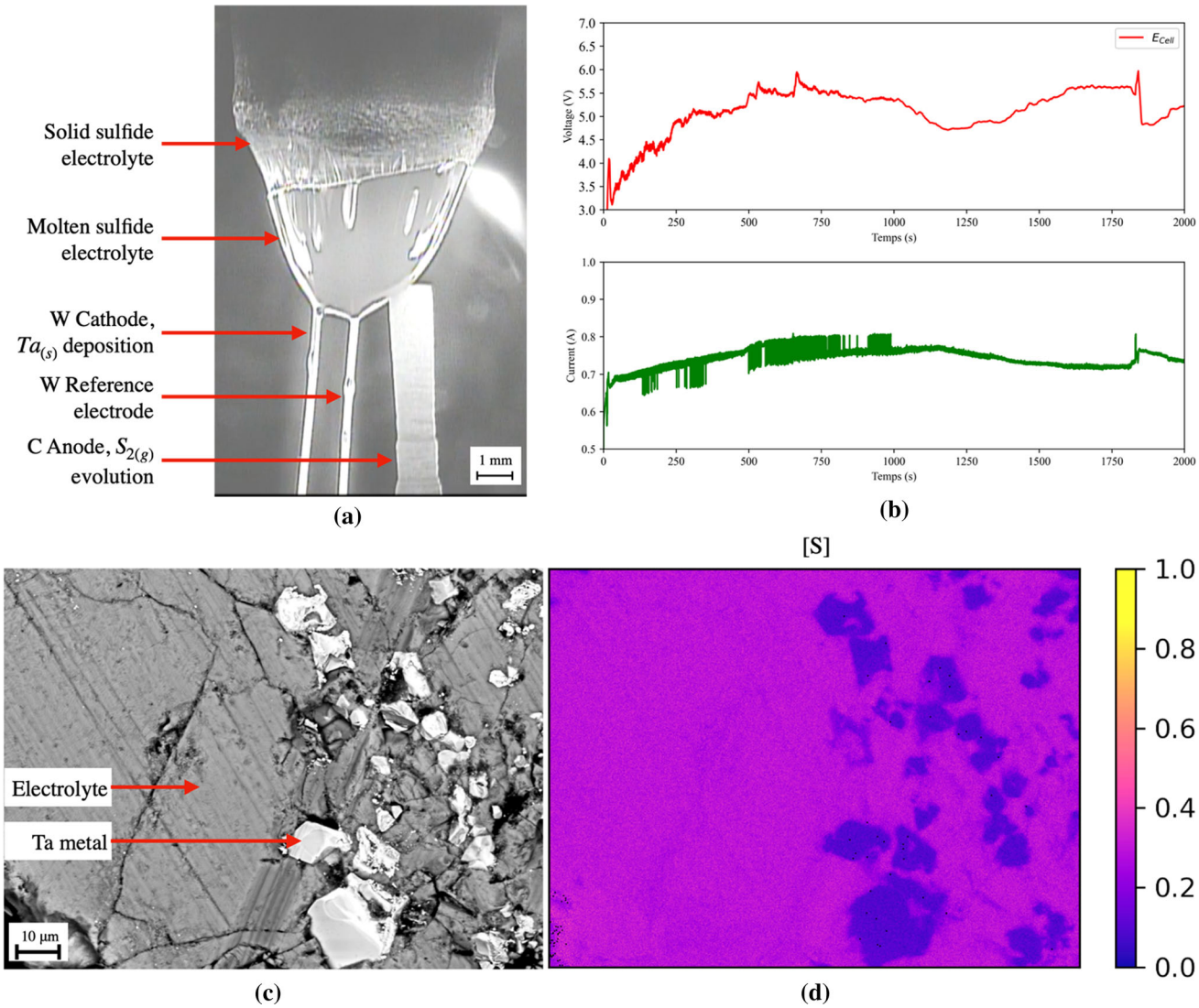

Fig. 14—(*a*) Pendant droplet electrolysis set-up with electrodes inserted; (*b*) chronoamperometry at an applied potential of 0.8 V *vs* W reference, total cell voltage (red), and corresponding current (green); (*c*) SEM/BEC images of a horizontal cross section of the electrolyte post-chronoamperometry; (*d*) map of EDS point analysis for elemental sulfur distribution (Color figure online).

3. The nitric acid leaching step is comparable to existing industrial processes, converting sulfides to sulfates. While not covered in this study, thermodynamic analyses suggest that $MnSO_4$ can form directly from MnS in the presence of Ta_2O_5 under controlled p_{S_2}/p_{SO_2}. This acid leaching step could then potentially be bypassed through selective sulfidation followed by selective sulfatation.

IV. CONCLUSION

A new process route for tantalum oxide capacitors recycling *via* sulfide chemistry is presented. The capacitor treatment allowed the removal of the epoxy mold, silica, metallic leads, and metallic frame *via* calcination and physical separation. A ternary oxide $MnTa_2O_6$ was formed during the calcination step. The remainder of the treatment isolated this ternary oxide powder from the other components of the capacitors.

The selective sulfidation of $MnTa_2O_6$ then allowed the breakage of the ternary oxide structure into a mix of manganese sulfide and tantalum oxide. Some possible limitations in conversion were identified and overcome, confirming the key leveraging role of the p_{S_2}/p_{SO_2} ratio during sulfidation. Manganese sulfide was leached in a nitric acid solution along other metallic sulfide impurities, and a single, high-purity orthorhombic Ta_2O_5 phase was obtained.

As a proof of concept, the sulfidation of Ta_2O_5 into TaS_2 was also demonstrated, highlighting the need for dedicated models, likely hybrid of the shrinking core and homogenous models. The electro-reduction of TaS_2 in a molten sulfide electrolyte was presented for the first time. Metallic tantalum particles and anodic gas

evolution were observed. Overall, the process may support the production of metallic tantalum powder without dependence on the conventional K-salt route.

ACKNOWLEDGMENTS

This work was financially supported by the U.S.A. Defense Advanced Research Projects Agency, under Agreement HR00112290087. The authors wish to thank Dr. Caspar Stinn, Mr. Ethan Benderly-Kremen, and Mrs. Sophie De Raedemacker for their insights and assistance.

AUTHOR CONTRIBUTIONS

CB conducted the research conceived with advising from AA. CB wrote the manuscript with edits from AA. All authors reviewed the manuscript.

FUNDING

Open Access funding provided by the MIT Libraries.

COMPETING INTERESTS

The authors declare no competing interests.

SUPPLEMENTARY INFORMATION

The online version contains supplementary material available at https://doi.org/10.1007/s11663-024-03427-1.

REFERENCES

1. R. Linnen, D.L. Trueman, and R. Burt: *Critical Metals Handbook*, 1st ed., G. Gunn, ed., Wiley, 2014, pp. 361–84.
2. J.W. Arblaster: *J. Phase Equilib. Diffus.*, 2018, vol. 39(2), pp. 255–72.
3. A.J. Padilla and N.T. Nassar: *Resour. Conserv. Recycl.*, 2023, vol. 190, 106783.
4. A.J. Padilla: *Tantalum: Mineral Commodity Summaries*, U.S. Geological Survey, 2020.
5. N.A. Mancheri, B. Sprecher, S. Deetman, S.B. Young, R. Bleischwitz, L. Dong, R. Kleijn, and A. Tukker: *Resour. Conserv. Recycl.*, 2018, vol. 129, pp. 56–69.
6. D. Moran, D. McBain, K. Kanemoto, M. Lenzen, and A. Geschke: *J. Ind. Ecol.*, 2015, vol. 19(3), pp. 357–65.
7. R. Bleischwitz, M. Dittrich, and R. Pierdicca: *Resour. Policy*, 2012, vol. 37(1), pp. 19–29.
8. E.L. Koerner and M. Smutz: *Separation of Niobium and Tantalum - A Literature Survey*, United States Atomic Energy Commission, 1956, pp. 1–14.
9. M. Nete, W. Purcell, and J.T. Nel: *Hydrometallurgy*, 2014, vol. 149, pp. 31–40.
10. J. Cui and L. Zhang: *J. Hazard. Mater.*, 2008, vol. 158, pp. 228–56.
11. H. Wang, S. Zhang, B. Li, D. Pan, Y. Wu, and T. Zuo: *Resour. Conserv. Recycl.*, 2017, vol. 126, pp. 209–218.
12. H. Ramon, J.R. Peeters, W. Sterkens, J.R. Duflou, K. Kellens, and W. Dewulf: *Procedia CIRP*, 2020, vol. 90, pp. 421–25.
13. B. Choi, B. Domínguez, A. D'Souza, H. Khadse, A. Kunkel, S. Nagarajan, T. Necke, R. Peche, M. Revello, J. Rossa, F. Sauer, S. Huyer, O. Schulz, S. Vorwerg, C. Walls, M. Wickleder, and G. Beck: *Resour. Conserv. Recycl.*, 2023, vol. 198, 107201.
14. K. Mineta and T.H. Okabe: *J. Phys. Chem. Solids*, 2005, vol. 66, pp. 318–21.
15. M. Agrawal, R. Singh, M. Ranitović, Z. Kamberovic, C. Ekberg, and K.K. Singh: *Sustain. Mater. Technol.*, 2021, vol. 29, e00323.
16. L.S. Von Brisinski, D. Goldmann, and F. Endres: *Chem. Ing. Technol.*, 2014, vol. 86(1–2), pp. 196–99.
17. S. Katano, T. Wajima, and H. Nakagome: *APCBEE Proc.*, 2014, vol. 10, pp. 182–86.
18. T. Fujita, H. Ono, G. Dodbiba, and K. Yamaguchi: *Waste Manage.*, 2014, vol. 34(7), pp. 1264–73.
19. B. Niu, Z. Chen, and Z. Xu: *J. Clean. Prod.*, 2017, vol. 166, pp. 512–18.
20. B. Niu, Z. Chen, and Z. Xu: *J Hazard. Mater.*, 2017, vol. 335, pp. 39–46.
21. B. Niu, Z. Chen, and Z. Xu: *ACS Sustain. Chem. Eng.*, 2017, vol. 5(2), pp. 1376–81.
22. W.-S. Chen, H.J. Ho, and K.Y. Lin: *Materials*, 2019, vol. 12(8), p. 1220.
23. W.-S. Chen, C.-Y. Hsiao, and C.-H. Lee: *Materials*, 2022, vol. 15(2), p. 656.
24. B. Niu, Z. Chen, and Z. Xu: *ACS Sustain. Chem. Eng.*, 2017, vol. 5(3), pp. 2639–47.
25. M. Sasaki, S. Ishikawa, K. Nasu, A.T. Quitain, and M. Goto: *6th International Symposium on Feedstock Recycling of Polymeric Materials*, 2011, pp. 147–48.
26. B. Niu, Z. Chen, and Z. Xu: *ACS Sustain. Chem. Eng.*, 2017, vol. 5(5), pp. 4421–28.
27. M. Agrawal, R. Singh, and K.K. Singh: *J. Environ. Chem. Eng.*, 2022, vol. 10(4), pp. 108182–94.
28. M. Agrawal, R. Jha, K.K. Singh, and R. Singh: *Proceedings of the 3rd International Conference on Advances in Materials Processing: Challenges and Opportunities*, 2023, pp. 213–18.
29. A.C. Turnock: *Can. Miner.*, 1966, vol. 8, pp. 461–70.
30. N.V. Chukanov, M. Pasero, S.M. Aksenov, S.N. Britvin, N.V. Zubkova, L. Yike, and T. Witzke: *Miner. Mag.*, 2023, vol. 87(1), pp. 18–33.
31. N. Schönberg: *Acta Metall.*, 1955, vol. 3(1), pp. 14–16.
32. S. Esmaeilzadeh and J. Grins: *Solid State Sci.*, 2002, vol. 4(1), pp. 117–23.
33. N.V. Tarakina, A.P. Tyutyunnik, V.G. Zubkov, T.V. D'Yachkova, Y.G. Zainulin, H. Hannerz, and G. Svensson: *Solid State Sci.*, 2003, vol. 5(7), pp. 983–94.
34. C.A. dos Santos, L.I. Zawislak, E.J. Kinast, V. Antonietti, and J.B.M. da Cunha: *Braz. J. Phys.*, 2001, vol. 31(4), pp. 616–31.
35. E.J. Kinast, O. Isnard, J.B.M. da Cunha, M.A.Z. de Vasconcellos, and C.A. dos Santos: *J. Appl. Crystallogr.*, 2011, vol. 44(4), pp. 738–46.
36. A.C. Turnock: *J. Am. Ceram. Soc.*, 1965, vol. 49(5), pp. 382–84.

37. H. Majima, Y. Awakura, M. Mashima, and T. Hirato: *Metall. Trans. B*, 1988, vol. 19B, pp. 355–63.
38. C. Stinn and A. Allanore: *Ni–Co 2021: The 5th International Symposium on Nickel and Cobalt*, 2021, pp. 99–110.
39. K.E. Daehn, C. Stinn, L. Rush, E. Benderly-Kremen, M.E. Wagner, C. Boury, B. Chmielowiec, C. Gutierrez, and A. Allanore: *Metals*, 2022, vol. 12(9), p. 1440.
40. C. Stinn and A. Allanore: *Rare Met. Technol.*, 2022, vol. 2022, pp. 259–78.
41. C. Boury, S.R. Green, and A. Allanore: *Metall. Mater. Trans. B.*, 2023, vol. 54B(6), pp. 3270–87.
42. S. Ahmad, M.A. Rhamdhani, M.I. Pownceby, and W.J. Bruckard: *Trans. Inst. Min. Metall. Sect. C Miner. Process. Extr. Metall.*, 2014, vol. 123(3), pp. 165–77.
43. J. Han, W. Liu, D. Wang, F. Jiao, and W. Qin: *Metall. Mater. Trans. B.*, 2016, vol. 47B(1), pp. 344–54.
44. T. Zhang, W. Liu, J. Han, G. Wu, F. Jiao, and W. Qin: *Sep. Purif. Technol.*, 2021, vol. 259, pp. 1–12.
45. P. Afanasiev, L. Fischer, F. Beauchesne, M. Danot, V. Gaborit, and M. Breysse: *Catal. Lett.*, 2000, vol. 64, pp. 59–63.
46. E. Ahmadi and R.O. Suzuki: *Metall. Mater. Trans. B.*, 2020, vol. 51B(1), pp. 140–48.
47. T. Kaneko, Y. Yashima, E. Ahmadi, S. Natsui, and R.O. Suzuki: *J. Solid-State Chem.*, 2020, vol. 285, 121268.
48. Z. Zeng, B.Z. Dlugogorski, and M. Altarawneh: *Fire Saf. J.*, 2017, vol. 91, pp. 226–34.
49. B. Zhang, L. Zhu, W. Liu, J. Han, F. Jiao, and W. Qin: *Metall. Mater. Trans. B.*, 2019, vol. 50B(2), pp. 761–71.
50. C. Stinn and A. Allanore: *Nature*, 2022, vol. 602(7895), pp. 78–83.
51. N.B. Pilling and R.E. Bedworth: *J. Inst. Met.*, 1923, vol. 29, pp. 529–91.
52. A.C. Turnock: *J. Am. Ceram. Soc.*, 1966, vol. 49(4), pp. 177–80.
53. A.C. Turnock: *J. Am. Ceram. Soc.*, 1965, vol. 48(5), pp. 258–61.
54. R.I. Gulyaeva, S.A. Petrova, V.M. Chumarev, and E.N. Selivanov: *J. Alloys Compd.*, 2020, vol. 834, 155153.
55. C. Boury and A. Allanore: *Sci. Rep.*, 2021, vol. 11(1), p. 18189.
56. C. Stinn, E. Benderly-Kremen, and A. Allanore: *Light Metals 2023*, ed. S. Broek, The Minerals, Metals & Materials Series, TMS, 2023, pp. 1195–203.
57. C.M. Hsiao and A.W. Schlechten: *J. Met.*, 1952, vol. 4(1), pp. 65–69.
58. A.H. Reidies: *Ullmann's Encyclopedia of Industrial Chemistry*, 6th ed., vol. 2, Wiley-VCH Verlag GmbH & Co. KGaA, Weinheim, 2012, pp. 223–44.
59. S.P. Garg, N. Krishnamurthy, A. Awasthi, and M. Venkatraman: *J. Phase Equilib.*, 1996, vol. 17(1), pp. 63–77.
60. T.H. Elmer and M.E. Nordberg: *J. Am. Ceram. Soc.*, 1958, vol. 41(12), pp. 517–20.
61. M. Ishida and C.Y. Wen: *AlChE J.*, 1968, vol. 14(2), pp. 311–17.
62. H.Y. Sohn: *Can. J. Chem. Eng.*, 2019, vol. 97, pp. 2061–67.
63. J. Cho and H.Y. Sohn: *Can. J. Chem. Eng.*, 2016, vol. 94, pp. 1516–23.
64. L.A. Aleshina and S.V. Loginova: *Crystallogr. Rep.*, 2002, vol. 47(3), pp. 415–19.
65. F. Jellinek: *J. Less Common Met.*, 1962, vol. 4, pp. 9–15.
66. A. Meetsma, G.A. Wiegers, R.J. Haange, and J.L. de Boer: *Acta Crystallogr. C*, 1990, vol. 46(9), pp. 1598–99.
67. Q. Dehaine, Y. Foucaud, J.S. Kroll-Rabotin, and L.O. Filippov: *Sep. Purif. Technol.*, 2019, vol. 215, pp. 590–601.
68. D. Chipfunhu, G. Bournival, S. Dickie, and S. Ata: *Miner. Eng.*, 2019, vol. 131, pp. 272–79.